

Fourier-over-spheroid shape parametrization applied to nuclear fission dynamicsK. Pomorski ^{1,*}, B. Nerlo-Pomorska,¹ C. Schmitt ², Z. G. Xiao,^{3,†} Y. J. Chen ⁴ and L. L. Liu⁴¹*Uniwersytet Marii Curie Skłodowskiej, Katedra Fizyki Teoretycznej, 20031 Lublin, Poland*²*IPHC, University of Strasbourg, 67200 Strasbourg, France*³*Department of Physics, Tsinghua University, Beijing 100084, China*⁴*China Institute of Atomic Energy, Beijing 102413, China*

(Received 5 March 2023; accepted 7 April 2023; published 26 May 2023)

We propose a new, rapidly convergent shape parametrization, the so-called Fourier-over-spheroid (FoS) approach, to model fission of heavy nuclei. Four collective coordinates are used to characterize the shape of the fissioning system: its elongation, left-right asymmetry, neck size, and nonaxiality. The potential energy landscape is computed within the macroscopic-microscopic approach, on the top of which the multidimensional Langevin equation is solved to describe the dynamics. Charge equilibration at scission and deexcitation of the primary fragments after scission are further considered. The model gives access to a wide variety of observables, including fission fragments' mass, charge, and kinetic energy yields, fragment mean N/Z and postscission neutron multiplicities, and, importantly, their correlations. The latter are crucial to unravel the complexity of the fission process. The parameters of the model were tuned to reproduce experimental observation from thermal neutron-induced fission of ^{235}U , and next used to discuss the transition from the asymmetric to symmetric fission along the Fm isotopic chain.

DOI: [10.1103/PhysRevC.107.054616](https://doi.org/10.1103/PhysRevC.107.054616)**I. INTRODUCTION**

Fission is a dynamical process during which a nucleus progressively deforms (either spontaneously or triggered by an external perturbation) from an initial compact configuration until a point where it splits into two fragments. This evolution is an intricate puzzle, involving a complex rearrangement of the many-body neutron and proton quantum systems. Intense effort has been invested in fission studies since its discovery, on both the experimental and theoretical fronts, due to the impact on fundamental nuclear physics and astrophysics, as well as for a wide variety of societal applications.

Modeling fission, in general, implies four stages: (i) the definition of the initial conditions of the system, (ii) its dynamical evolution, and rearrangement in specific configurations of fragment pairs with corresponding probabilities, (iii) the (fast) prompt deexcitation of the excited fragments, and (iv) the (slow) decay towards β stability of those fragments which are radioactive. The recent review by Schunck and Regnier [1] gives an excellent panorama on contemporary fission theories, and further details about foundations can be found in the textbook by Krappe and Pomorski [2]. In spontaneous and low-energy (mostly induced by neutrons) fission, the initial conditions are well defined. The radioactive decay of the fission products is well known also. To understand fission, the challenge thus mainly resides in the description of stages (ii) and (iii). These are not independent each other: Stage (iii) critically depends on the properties (N , Z , excitation energy,

and angular momentum) of the (primary) fragments produced at scission at the end of stage (ii).

While experimental information was restricted to fission-fragment mass distributions with limited resolution for several decades [3], recent developments give access to a widespread variety of observables and their correlations, with unprecedented resolution [4–8]. Such information is essential to unravel in an un-ambiguous way the intricacies of the fission process. It is obviously of primary importance for constraining theory, but it poses also a tremendous challenge, which is the requirement of modeling all aspects of the mechanism and their mutual interdependences.

According to the complexity of the fission process, its description remains a challenge for theory, and various models have been proposed over the years. The last decade has seen the tremendous development of microscopic, self-consistent models. Unfortunately, the quantitative description remains limited so far, and computing time makes systematic calculations impossible even with supercomputers [1]. Transport models within the macroscopic-microscopic approach have been established as a very good alternative. In this framework, the process is given by the solution of a classical equation of motion picturing the real-time evolution of the system on its potential energy landscape (PEL) under the influence of inertia, dissipation, and fluctuations [9]. Systematic studies covering different regions of the nuclear chart are nowadays computationally tractable. Such widespread investigations are indispensable to converge towards a universal understanding of the process [10].

Sophisticated macroscopic-microscopic models based on the solution of the multidimensional Langevin equation, or some variant of it, were developed during the last two decades

*pomorski@kft.umcs.lublin.pl

†xiaozg@mail.tsinghua.edu.cn

[1,11]. In these models, three main ingredients are required: a parametrization of the nuclear shape involving as few as possible deformation coordinates, a prescription for the potential energy of the nucleus, and a modelization for inertia and friction forces. Aritomo *et al.* [12] and Usang *et al.* [13] developed, respectively, three- and four-dimensional (3D and 4D) dynamical models to explain fragment mass and total kinetic energy (TKE) distributions in spontaneous and low-energy fission. Unfortunately, these models do not compute the postscission deexcitation of the fragments. Furthermore, the hypothesis of unchanged charge density (UCD), i.e., the fragments have the same N/Z ratio as the fissioning system, is assumed in the model of Aritomo *et al.* Finally, evaporation prior to scission (so-called multichance fission) is not considered, making these codes unsuited for fissioning system initial excitation energy above 10 MeV or so [14]. The Brownian shape motion model by Randrup and Möller [15] is based on the current highest-quality 5D potential energy landscapes. While its enhanced version by Albertsson *et al.* [16] adds the postscission stage, similarly to the early code, the UCD assumption is made. Möller and Ichikawa [17] went beyond this hypothesis, treating independently neutrons and protons, which renders the model 6D. Unfortunately, this version is still to be combined with the postscission stage of Ref. [16]. Furthermore, as in Refs. [12,13] the possibility of multichance fission is not implemented. In our previous works [18,19], we developed an innovative nuclear shape parametrization, the Fourier parametrization, which demonstrated gathering within 4 collective coordinates the main features of the shapes relevant to fission. The new shape parametrization was successfully used within the Born-Oppenheimer approximation [20] to describe fission fragment mass yields [21,22]. We further implemented this parametrization (restricted to 3D), with a suited PEL prescription, and inertia and friction forces borrowed from classical mechanics, into a Langevin code. The latter was able to reasonably describe fragment mass and TKE distributions from low-energy fission of typical actinides [23]. It was used also for predictions in the superheavy element region [24]. The present work is a twofold extension of these papers. First, we present an enhanced version of our shape parametrization, called Fourier over spheroid (FoS) [25,26]. Second, we develop the previous Langevin code by proposing a method to compute (i) the fragments' (N, Z) compositions, i.e., leveling off the UCD assumption, and (ii) their properties in terms of excitation energy and deformation at the instant of scission.¹ This information is finally used as input in the extension of the code to the calculation of the postscission stage. Altogether we offer a demonstration of a particularly fast and flexible way to compute a wide variety of observables. Comparison with experiment is made wherever possible for spontaneous and low-energy fission. Although not treated in this paper, work to account for multichance fission is in progress.

II. MODEL

In this section the various ingredients entering in the here-developed model are presented. Thermal neutron-induced fission of ^{235}U is taken as an example to illustrate the main features of the theory and the variety of observables computed by the code. In Sec. III the model is applied to spontaneous fission of fermium.

A. Nuclear shape parametrization

The surface of the fissioning nucleus is described in the cylindrical coordinates (ρ, φ, z) by the following formula [26]:

$$\rho^2(z, \varphi) = \frac{R_0^2}{c} f\left(\frac{z - z_{\text{sh}}}{z_0}\right) \frac{1 - \eta^2}{1 + \eta^2 + 2\eta \cos(2\varphi)}, \quad (1)$$

where $\rho(z, \varphi)$ is the distance from the z axis to the surface. Function $f(u)$ defines the shape of the nucleus having half-length $c = 1$:

$$f(u) = 1 - u^2 - \sum_{k=1}^n \left\{ a_{2k} \cos\left(\frac{k-1}{2}\pi u\right) + a_{2k+1} \sin(k\pi u) \right\}, \quad (2)$$

where $-1 \leq u \leq 1$ and the expansion coefficients a_i are treated as the deformation parameters. The first two terms in $f(u)$ describe a sphere. The volume conservation condition implies $a_2 = a_4/3 - a_6/5 + \dots$. The parameter c determines the elongation of the nucleus, keeping its volume fixed, while a_3 and a_4 describe the reflectional asymmetry and the neck size, respectively. The half-length is $z_0 = cR_0$, where R_0 is the radius of a sphere with the same volume. The z coordinate varies in the range $-z_0 + z_{\text{sh}} \leq z \leq z_0 + z_{\text{sh}}$. The shift $z_{\text{sh}} = -3/(4\pi)z_0(a_3 - a_5/2 + \dots)$ places the mass of the nucleus at the origin of the coordinate system. The parameter η describes a possible elliptical, nonaxial deformation of a nucleus.

The formula (1) is entirely equivalent to those based on the Fourier expansion and described in Refs. [19]. Here, the deviation from a sphere with radius $\rho = 1$ is first expanded in the Fourier series, and subsequently this deformed object the length $2R_0$ is scaled to the elongation equal to $2cR_0$. The formula (1) is more adapted to the calculation of the PEL of nuclei made on a mesh in the multidimensional deformation parameter $(c, a_3, a_4, \dots, a_n)$ space since the range of variability of the a_i coefficients does not depend on the elongation c . In addition, the mass ratio of the fragments, their relative distance, and the radius of the neck between them, measured in z_0 units, do not depend on the elongation of the nucleus. It is also worth noticing that, for the reflection symmetric shapes, the geometrical scission points appear when $a_4 = a_4^{\text{sc}} = \frac{3}{4} + \frac{6}{5}a_6 + \dots$ independently of the elongation c . Such properties of the present FoS shape parametrization make it very useful for all kinds of calculations related to nuclear fission.

The PELs of fissioning nuclei are obtained in the 4D space of deformation parameters (c, a_3, a_4, η) using the macro-micro model [27]. The macroscopic part of the energy is evaluated according to the Lublin-Strasbourg drop (LSD) formula [28], while the microscopic energy correc-

¹At present, the angular momentum of the fragments is not treated in the model.

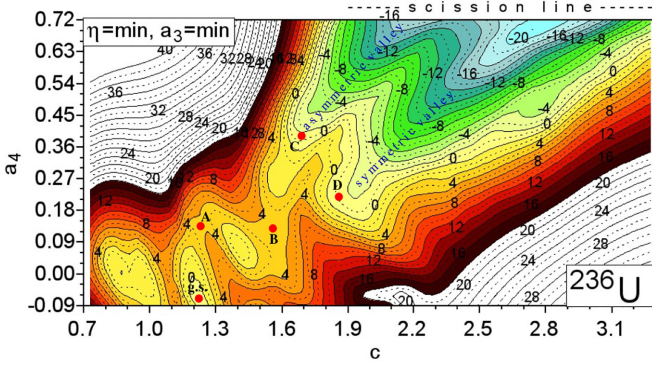


FIG. 1. Potential energy surface of ^{236}U on the (c, a_4) plane for the temperature $T = 0$. Each point is minimized with respect to the nonaxial (η) and the reflectional (a_3) deformations.

tions are calculated using the Yukawa-folded single-particle potential [29] and the Strutinsky shell correction method [27,30]. The pairing correlations are described using the BCS formalism [31] using an approximative projection on a good particle number [32,33]. All parameters of the macro-micro model used in the present paper are the same as in Ref. [34].

A typical PEL of the ^{236}U fissioning nucleus, as an example, is shown in Fig. 1. It is a projection of the 4D PEL onto the (c, a_4) plane, i.e., each energy point in the (c, a_4) map is minimized with respect to the nonaxial η and reflectional a_3 deformation parameters. The ground state (g.s.) and the first (A) and second (B) saddle points are marked in the plot. Beyond the second saddle B, two separate paths develop, an asymmetric one and a symmetric one. The exit points from the fission barrier leading to the asymmetric (C) and symmetric (D) fission valleys are also marked. The upper value of the neck parameter $a_4 = 0.72$ corresponds to a neck radius approximately equal to the nucleon radius, $r_{\text{neck}} = r_0$, which we assume in the following as the scission criterion. Here r_0 is the nucleus radius constant. The nonaxial degree of freedom is important at a smaller elongation of the nucleus until the neighborhood of the second saddle. At larger deformation, its effect is negligible, allowing us to restrict the Langevin calculations to 3D when discussing fission dynamics. Moreover, the role of the higher-order deformation parameters a_5 and a_6 is rather small even in the region of well-separated fission fragments, as shown in Ref. [24]. The (c, A_h) cross section of the PEL of ^{236}U at $a_4 = 0.72$ is presented in Fig. 2. This cross section corresponds roughly to scission ($r_{\text{neck}} \simeq r_0$), as noted above. Here A_h is the heavy fragment mass number. The close-to-scission configuration of the asymmetric valley evidenced in Fig. 1 corresponds to the minimum at $A_h = 140$ and $c = 2.2$, while the end of the symmetric valley of Fig. 1 occurs at $c = 2.83$. As expected, asymmetric fission of uranium leads to a more compact scission configuration compared to symmetric splitting.

B. Dynamical evolution

The Langevin equation governs the dissipative fission dynamics. In the generalized coordinates ($\{q_i\}$, $i = 1, 2, \dots, n$)

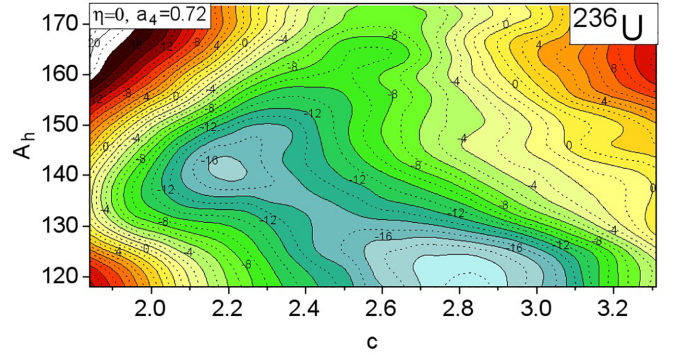


FIG. 2. Potential energy surface of ^{236}U around the scission configuration ($a_4 = 0.72$) on the (c, A_h) plane for the temperature $T = 0$. Each point is minimized with respect to the nonaxial (η) deformations.

it has the following form [2]:

$$\begin{aligned} \frac{dq_i}{dt} &= \sum_j [\mathcal{M}^{-1}(\vec{q})]_{ij} p_j \\ \frac{dp_i}{dt} &= -\frac{1}{2} \sum_{j,k} \frac{\partial [\mathcal{M}^{-1}]_{jk}}{\partial q_i} p_j p_k - \frac{\partial V(\vec{q})}{\partial q_i} \\ &\quad - \sum_{j,k} \gamma_{ij}(\vec{q}) [\mathcal{M}^{-1}]_{jk} p_k + F_i(t), \end{aligned} \quad (3)$$

Here $V(\vec{q}) = E_{\text{pot}}(\vec{q}) - a(\vec{q})T^2$ is the free energy of a fissioning nucleus having temperature T and the single-particle level density $a(\vec{q})$. The potential energy $E_{\text{pot}}(\vec{q})$ at a given deformation point (\vec{q}) is given by the macroscopic-microscopic prescription quoted in the previous section, and the level density $a(\vec{q})$ at corresponding deformation is taken from Ref. [35]. The inertia \mathcal{M}_{jk} and the friction γ_{ij} tensors are evaluated in the irrotational flow and the wall approximation, respectively, as described in Refs. [24,36].

The vector $\vec{F}(t)$ stands for the random Langevin force, which couples the collective dynamics to the intrinsic degrees of freedom and is defined as

$$F_i(t) = \sum_j g_{ij}(\vec{q}) G_j(t), \quad (4)$$

where $\vec{G}(t)$ is a stochastic function whose strength $g(\vec{q})$ is given by the diffusion tensor $\mathcal{D}(\vec{q})$ defined by the generalized Einstein relation

$$\mathcal{D}_{ij} = T^* \gamma_{ij} = \sum_k g_{ik} g_{jk}, \quad (5)$$

where

$$T^* = E_0 / \tanh\left(\frac{E_0}{T}\right). \quad (6)$$

Here $E_0 = 3 \times 0.5$ MeV is the zero-point collective energy. The temperature T is obtained from the thermal excitation energy E^* defined as the difference between the initial energy (E_{init}) and the total collective energy, which is the sum of the kinetic (E_{kin}) and potential (V) energies of the fissioning

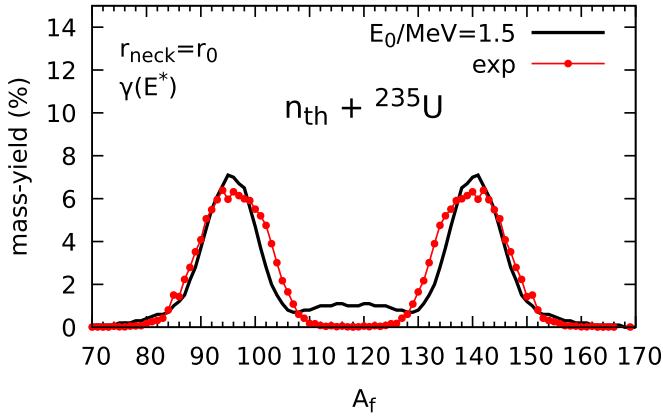


FIG. 3. Fission fragment mass yield of $n_{\text{th}} + {}^{235}\text{U}$ as a function of the mass of the fragment. The experimental data are taken from Ref. [37].

nucleus at a given deformation point (\bar{q}):

$$a(\bar{q})T^2 = E^*(\bar{q}) = E_{\text{init}} - (E_{\text{kin}} + V). \quad (7)$$

For a given fissioning system, several thousand Langevin trajectories leading to scission are run. From such samples, the properties of the primary fragments are evaluated, giving the mass and kinetic energy distributions presented below.

1. Mass yields

The primary or so-called preneutron fission fragment mass yield, as obtained for thermal neutron-induced fission of ${}^{235}\text{U}$, is shown in Fig. 3. Note that it was assumed here that each Langevin trajectory begins randomly at the region of the second saddle (B) with the half-width of the initial distribution equal to the distance between the mesh points ($\delta q_i = 0.03$). It was observed that this leads to a predicted mass yield of ${}^{236}\text{U}$ which is almost independent of the starting point: similar mass distributions are obtained when starting from the ground state deformation or from the first saddle (A). Our result describes pretty well the maxima and the tails of the experimental mass yield at large asymmetry [37]. However, the yield at symmetry is slightly overestimated.

2. Total kinetic energy

For each Langevin trajectory, the total kinetic energy (TKE) of the fragments $E_{\text{kin}}^{\text{frag}}$ is given by the sum of the Coulomb repulsion energy (V_{Coul}), the nuclear interaction energy of fragments (V_{nuc}), and the prefission kinetic energy of the relative motion ($E_{\text{kin}}^{\text{Coll}}$) evaluated at the scission point (q_{sc}):

$$E_{\text{kin}}^{\text{frag}} = V_{\text{Coul}}(q_{\text{sc}}) + E_{\text{kin}}^{\text{coll}}(q_{\text{sc}}) + V_{\text{nuc}}(q_{\text{sc}}). \quad (8)$$

The Coulomb repulsion energy is equal to the difference between the total Coulomb energy of the nucleus at the scission configuration and the Coulomb energies of both deformed fragments:

$$V_{\text{Coul}} = \frac{3e^2}{5r_0} \left[\frac{Z^2}{A^{1/3}} B_C(\bar{q}_{\text{sc}}) - \frac{Z_h^2}{A_h^{1/3}} B_C(\bar{q}_h) - \frac{Z_l^2}{A_l^{1/3}} B_C(\bar{q}_l) \right], \quad (9)$$

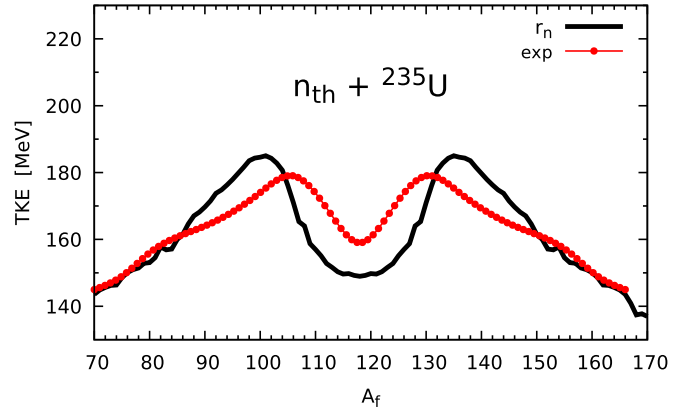


FIG. 4. Total kinetic energy yield of $n_{\text{th}} + {}^{235}\text{U}$ as a function of the mass of the fragment. The experimental data are taken from Ref. [5].

where $r_0 = 1.217$ fm is the same charge radius as in the LSD mass formula [28] and B_C is the ratio of the Coulomb energies of the deformed and spherical nuclei.

The nuclear interaction between the fragments at the scission point is approximately equal to the change of the nuclear surface energy when the neck breaks:

$$\begin{aligned} V_{\text{nuc}}(q_{\text{sc}}) &= -2 \times E_{\text{surf}}(0) \frac{\pi r_{\text{neck}}^2(\text{sc})}{4\pi R_0^2} \\ &= -\frac{1}{2} E_{\text{surf}}(0) \left(\frac{r_{\text{neck}}}{R_0} \right)^2. \end{aligned} \quad (10)$$

Here $E_{\text{surf}} = b_{\text{surf}} A^{2/3}$, where b_{surf} is the surface tension LD coefficient. For $r_{\text{neck}} = r_0$ and the nucleus radius $R_0 = r_0 A^{1/3}$ one obtains $V_{\text{nuc}}(q_{\text{sc}}) = -\frac{1}{2} b_{\text{surf}}$, i.e., $V_{\text{nuc}}(q_{\text{sc}}) \approx -9$ MeV for the neck radius equal to the nucleon radius. We note that this prescription for $E_{\text{kin}}^{\text{frag}}$ is undoubtedly a more accurate estimate of the fission-fragment kinetic energy than the frequently used point-charge approximation, $E_{\text{kin}} = e^2 Z_h Z_l / R_{12}$, where R_{12} is the distance between the fragment mass centers.

The mean TKE as a function of fragment mass as obtained from the model is compared in Fig. 4 with the experimental data [5]. These are reproduced well on average. Some discrepancy is noted though. First, the predicted TKE around $A_h = 140$ is too large. The yield in this mass region is nevertheless well described; see Fig. 3. Thus, we ascribe the discrepancy in TKE to the limitation of the 4D parametrization in describing the scission shapes characteristic of the so-called Standard II mode, corresponding to a deformed heavy fragment and a slightly or even close to spherical light partner [3]. Second, the maximum of the calculated TKE, expected to occur for the Standard I mode with a heavy fragment in the vicinity of ${}^{132}\text{Sn}$, is seen to be shifted to larger masses around $A_h = 136$. The reason for this discrepancy is twofold: (i) the difficulty of describing in a 4D deformation space the compact shapes characteristic of Standard I mode, and (ii) the too large contribution of the symmetric mode, noted already in Fig. 3, in the $A_h \approx 130$ region, which corresponds to very elongated scission shapes, and thus lowers the average TKE in this region.

C. Charge equilibration at scission

At the end of the Langevin trajectory, once the system has reached the scission point, the mass of the two fragments is determined by integrating the volume of the shapes at the left and right of the point of rupture. In the wide majority of macroscopic-microscopic models available, the isotopic composition, equivalently N/Z ratio, of the fragments is next assumed to be identical to the one of the fissioning nucleus (see, e.g., [12,15,16,23,24]). The UCD assumption was recently levelled off by Möller and Ichikawa [17] in a “6D” model by computing the probability of proton transfer between the two fragments along the dynamical evolution. In the fully microscopic approach, neutron and proton sharing at scission can in principle be obtained from the corresponding density distributions; see, e.g., Ref. [38] for a recent discussion. In the present work, we go beyond the UCD assumption which we employed in our previous model [23,24] as follows.

Starting from the fragment deformation at scission, we determine for each fragment mass the most probable charge based on the LSD energy and the pairing correlation energy. Such charge equilibration can be determined by looking at the change of the total energy of the fissioning system with the charge number of the heavy fragment Z_h :

$$\begin{aligned} E(Z, A, Z_h; A_h, \bar{q}_h, \bar{q}_l) \\ = E_{\text{LSD}}(Z_h, A_h; \bar{q}_h) \\ + E_{\text{LSD}}(Z - Z_h, A - A_h; \bar{q}_l) \\ + e^2 Z_h(Z - Z_h)/R_{12} - E_{\text{LD}}(Z, A; 0), \end{aligned} \quad (11)$$

where Z, A , and Z_h, A_h are the charge and mass numbers of the parent nucleus and the heavy fragment, respectively. The mass as well as the deformation parameters of the heavy (A_h, \bar{q}_h) and the light fragments (A_l, \bar{q}_l) are given by the division of the volume according to the shape of the nucleus at scission at the end of the Langevin trajectory, as mentioned in the previous work [23,24].

The total energy as a function of the fragment charge number is shown in the upper panel of Fig. 5. The odd-even energy (E_{odd}), taken from Ref. [28], is added to the LSD energy (E_{LSD}) for the odd proton of the fragment. The distribution of the heavy-fragment charge number can be estimated using a Wigner function corresponding to the energy E given by Eq. (11) for different values of Z_h :

$$W(Z_h) = \exp \left\{ - [E(Z_h) - E_{\text{min}}]^2 / E_W^2 \right\}, \quad (12)$$

which gives the distribution probability of the fragment charge shown in the bottom panel of Fig. 5. E_{min} in Eq. (12) is the lowest discrete energy as a function of Z_h . Furthermore, the following random number determines the charge number Z_h of the heavy fragment, with $Z_l = Z - Z_h$. The energy E_W should be comparable with the energy distance $\hbar\omega_0$ between harmonic oscillator shells since we have a single-particle (proton) transfer, here, between the touching fragments.

The above outlined prescription permits one to go beyond the UCD hypothesis by accounting for charge equilibration for a given mass split. The resulting fission fragment charge yield is compared with the data [39] in Fig. 6. As one can see, the odd-even effect for the most probable fission frag-

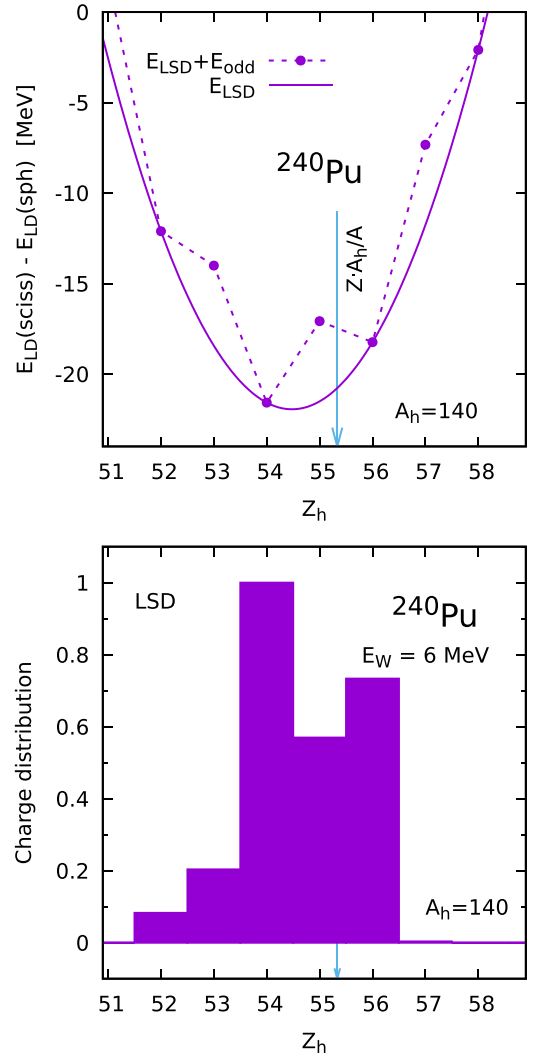


FIG. 5. Energy of ^{240}Pu at scission as a function of the heavy fragment charge number in the LSD mass formula [28] (top) and the Wigner distribution probability of the fragment charge number (bottom).

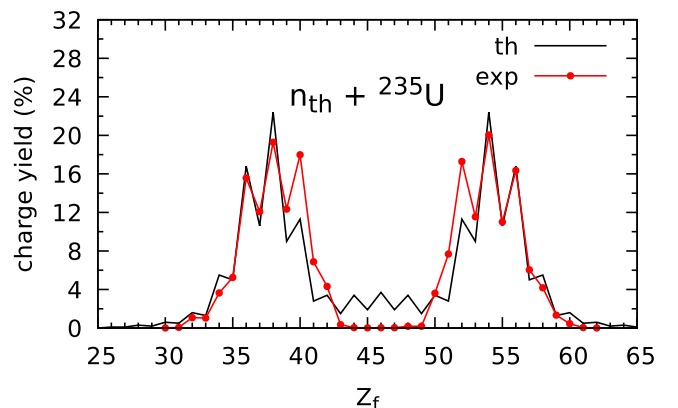


FIG. 6. Fission fragment charge yield of $n_{\text{th}} + ^{235}\text{U}$. The experimental data (red points) are taken from Ref. [39].

ment elements are well reproduced with our simple model, which is solely based on the LSD macroscopic energy, for the largest yields. Theory overestimates the staggering for most asymmetric splits and at symmetry. This dependence of the magnitude of the staggering with fragment charge is under intense debate [40] due to its connection with the influence of shell effects and dissipation in fission [41]. Within the present modeling, it will be the subject of future development. We note that a similar procedure could be introduced to account for neutron pairing. However, since evaporation after scission widely washes it out, it is hardly seen in experiment, and is not very exploitable.

D. Postscission evaporation

The primary fragments produced right at scission are in general excited. They return to their respective ground states by emitting neutrons and γ rays. Our previous model [23,24] was extended to account for postscission evaporation of neutrons. Competition with γ -ray emission has a negligible impact on neutron evaporation, as it occurs mostly below the fragment neutron separation energy. Inclusion of γ -ray emission is thus left for future development.

The excitation of the fissioning nucleus available at scission, and to be shared between the primary fragments, is evaluated as specified above with Eq. (7). It is then assumed that the thermal energy of a given fragment, E_i^* , at the scission point is proportional to its single-particle level density:

$$\frac{E_1^*}{E_h^*} = \frac{a(Z_1, A_1; \text{def}_1)}{a(Z_h, A_h; \text{def}_h)} \quad (13)$$

with $E^* = a(\bar{q})T^2 = E_1^* + E_h^*$ given by Eq. (7).

Since the fragments have usually a deformation at scission which differs from their equilibrium configuration, they very quickly relax to the ground-state shapes. The deformation energy released by this relaxation is transformed into excitation energy. The deformation energy of each fragment can be evaluated in the LD model [28]:

$$E_{\text{def}}^{(i)} \approx E_{\text{LD}}(Z_i, A_i, \text{def}_i) - E_{\text{exp}}(Z_i, A_i, \text{g.s.}). \quad (14)$$

The total excitation energy ($E_{\text{exc}}^{(i)}$) of fragment i is then the sum of its thermal and deformation energies:

$$E_{\text{exc}}^{(i)} = E_{\text{def}}^{(i)} + E_i^* = a(i)T_i^2. \quad (15)$$

For each fragment, this excitation energy is available for neutron emission.

The maximal energy of a neutron emitted from a fragment (parent) can be obtained from the energy conservation law:

$$\epsilon_n^{\text{max}} = M_M + E_M^* - M_D - M_n, \quad (16)$$

where M_M , M_D , M_n are the mass excesses of parent and daughter nuclei and of the neutron, respectively. These data can be taken from a mass table [42]. The thermal excitation energy of the daughter nucleus is

$$E_D^* = \epsilon_n^{\text{max}} - \epsilon_n. \quad (17)$$

Here ϵ_n is the kinetic energy of the emitted neutron.

The neutron emission probability for a (parent) fragment with excitation energy E_M^* is given by the

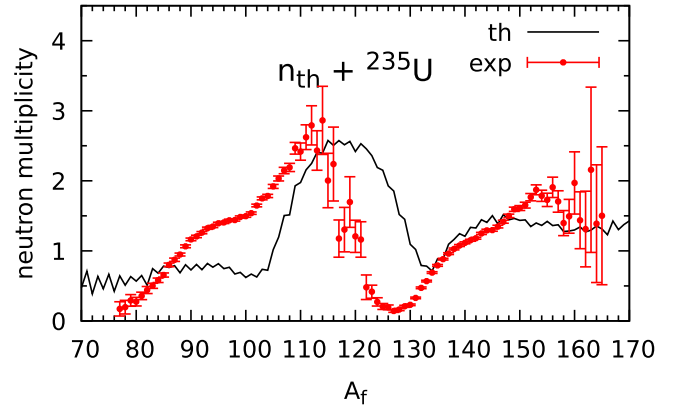


FIG. 7. Postscission neutron multiplicity as a function fragment mass for $n_{\text{th}} + {}^{235}\text{U}$. The experimental data (red points) are taken from Ref. [4].

Weißkopf formula [43]:

$$\Gamma_n(\epsilon_n) = \frac{2\mu}{\pi^2 \hbar^2 \rho_M(E_M^*)} \int_0^{\epsilon_n} \sigma_{\text{inv}}(\epsilon) \epsilon \rho_D(E_D^*) d\epsilon. \quad (18)$$

Here μ is the reduced mass of the neutron, σ_{inv} is the neutron inverse cross section [44],

$$\sigma_{\text{inv}}(\epsilon) = [0.76 + 1.93/A^{1/3} + (1.66/A^{2/3} - 0.050)/\epsilon] \pi (1.7A^{1/3})^2, \quad (19)$$

while ρ_M and ρ_D are, respectively, the level densities of parent and daughter nuclei:

$$\rho(E) = \frac{\sqrt{\pi}}{12a^{1/4}E^{5/4}} \exp(2\sqrt{aE}), \quad (20)$$

As in other parts of the model, the single-particle level density parameters a of the parent and the daughter are taken from Ref. [35].

Neutron evaporation is assumed to take place until the fragment reaches an excitation energy comparable to the neutron separation energy, for which we take an average value of 6 MeV (this energy is further exhausted by γ rays as also observed in experiment; see, e.g., Ref. [45]).

The number of neutrons emitted by the fragments as function of their mass is displayed in Fig. 7 and compared with the measurements [4]. The *sawtooth* shape observed in the experimental data is only roughly reproduced by the theoretical results. The too large multiplicity predicted in the range between $A \approx 116$ and 130 is partly due to the too large amount of very elongated scission shapes originating from the LD fission mode in this region, as already discussed in Fig. 3. The fragments of this mode experience a substantial shape relaxation after scission, which increases the excitation energy available for evaporation (see also Figs. 9 and 10). Furthermore, the too large amount of evaporation in the vicinity of ${}^{132}\text{Sn}$ is additionally due to the limitation of the model to describe the specific shapes of the Standard I mode. The small underprediction at $A \approx 155$ may similarly point out the issue of shape parametrization for those elongated heavy fragments. When the influence of structural effects in the heavy fragment dominates, energy minimization will naturally favor those

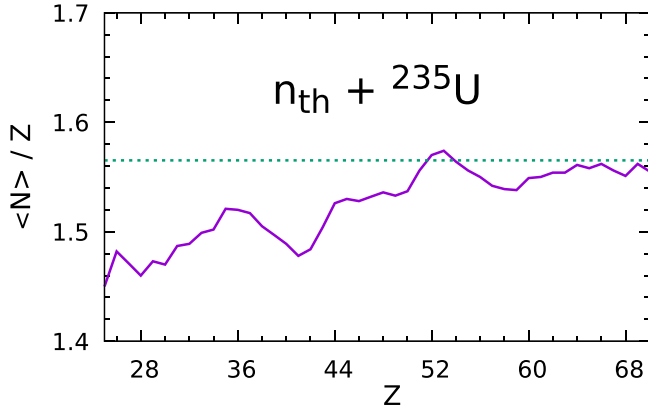


FIG. 8. Average postsission neutron to proton $\langle N \rangle / Z$ ratio for $n_{\text{th}} + {}^{235}\text{U}$. The dashed line represents the ratio of the compound nucleus.

pre-scission configurations which reproduce best the shape of the heavy “side” of the mononucleus approaching scission. The limited number of collective coordinates will necessarily bias the shape of the light counterpart and thus its excitation energy and postsission evaporation. That partly explains the discrepancy between theory and experiment in the region $A \approx (90\text{--}010)$. It is expected that inclusion of higher deformation parameters, namely a_5 and a_6 , which allow one to better control the fragments’ deformation, will substantially improve the description of postsission neutron multiplicities.

The average fragment neutron to proton ratio $\langle N \rangle / Z$ after postsission evaporation for fission of ${}^{236}\text{U}$ at thermal energies is shown in Fig. 8 as a function of the fragment charge number. The N/Z ratio of the initial system is given by the dashed line for reference. The change of the fragment $\langle N \rangle / Z$ with respect to the parent nucleus is due to charge equilibration at scission and postsission neutron evaporation. The general behavior observed in experiment (see, e.g., Ref. [7]), with the heavy fragment being relatively neutron rich and the lighter one neutron poor for fission of typical actinides, is reproduced. However, the influence of shell effects in the vicinity of ${}^{132}\text{Sn}$ is weaker in theory as compared to the measurement. As discussed above, we mostly attribute this to the limitation in the description of the particularly compact scission shapes characteristic of those fragmentations. The excitation of the heavy partner is then slightly overestimated and the neutron multiplicity gets too large, which lowers the $\langle N \rangle / Z$ ratio. To be best of our knowledge, apart from the present work, there are only two dynamical models that have addressed the experimentally observed evolution of $\langle N \rangle / Z$ with fragment charge (or mass): While the enhanced “6D” macroscopic-microscopic model of Möller and Ichikawa [17] achieved a very good quantitative description [46], the description by the self-consistent model of Verriere *et al.* [38] remained qualitative only.

The model developed in the present work calculates all fragment properties (except the angular momentum) in a consistent manner, and takes proper care of the correlations between the various quantities. For instance, the primary fragment N and Z distributions and associated shapes predicted by the calculation of the dynamical evolution up to the scis-

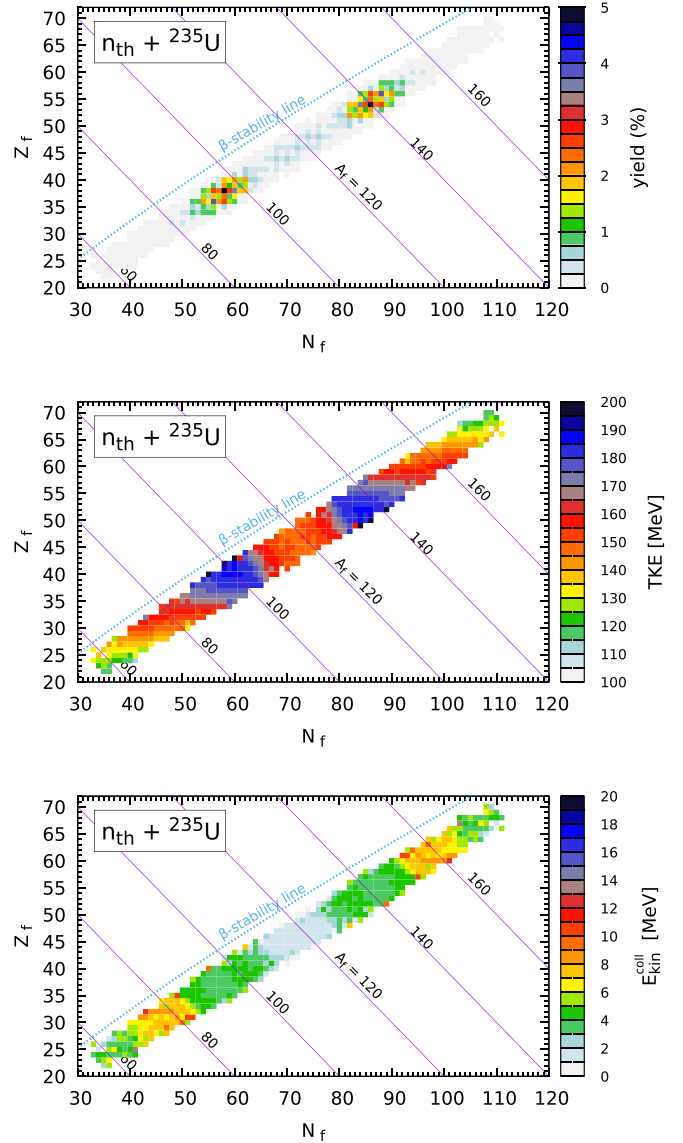


FIG. 9. Fission fragment yield (top), TKE (middle), and the pre-fission kinetic energy (bottom) for $n_{\text{th}} + {}^{235}\text{U}$ on the (N_f, Z_f) plane.

sion point determine the TKE. The primary (N, Z) population together with TKE gives the total excitation energy (TXE). The fragment deformation at scission together with the TXE enters the calculation of the intrinsic excitation energy of the fragments, which finally determines the neutron multiplicity and N/Z neutron excess. Correlations are essential to get further insight into the process, as well as to understand possible deviation between experiment and theory. The primary fragment yield, TKE, and the pre-fission kinetic energy $[E_{\text{kin}}^{\text{coll}}$, Eq. (8)] of ${}^{236}\text{U}$ are shown in Fig. 9 on the (N_f, Z_f) plane. In our model, the most probable primary fragments are ${}^{140}\text{Xe}$ and ${}^{96}\text{Sr}$, consistent with what was suggested by combining the experimental observations of Refs. [32,37,47]. The largest TKE $\gtrsim 190$ MeV corresponds to neutron-rich fragments with mass $A \approx 130\text{--}040$ and correlated with light fragments around $A = 100$ having smaller neutron excess. The pre-fission kinetic energy for the most probable fission fragments is only around

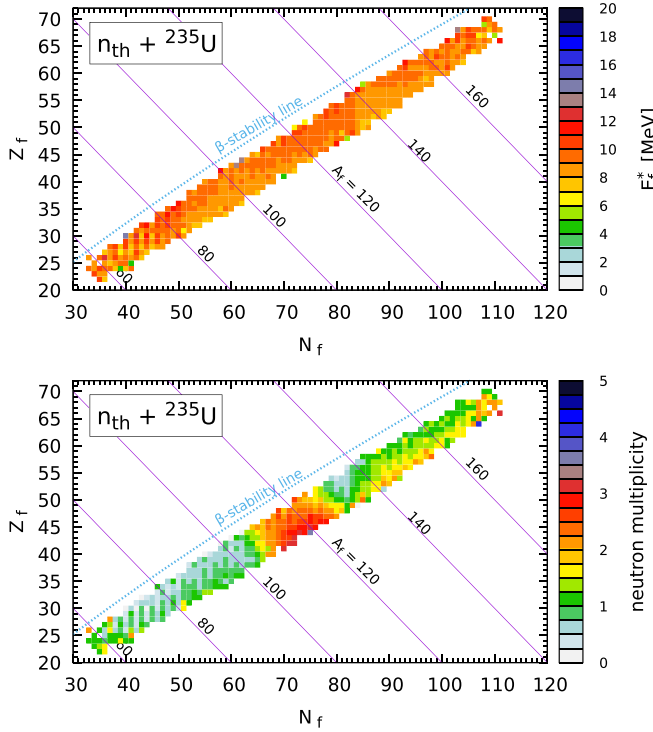


FIG. 10. Fission fragment excitation energy (top) and neutron multiplicity (bottom) for $n_{\text{th}} + {}^{235}\text{U}$ on the (N_f, Z_f) plane.

3 MeV. Rather small values of the TKE of the fragments, equal to approximately 140 MeV, are calculated for symmetric fission. The larger TKE for the Standard I and II modes as compared to the LD symmetric mode well established from experiment [47] is thus reproduced. However, the measured difference between Standard I and Standard II is not evident in the calculation, presumably due to the limited number of collective coordinates. That translates into a fragment excitation in the vicinity of ${}^{132}\text{Sn}$ which is somehow too large, and consequently an overestimation of the number of neutrons emitted, as noted above. This is indeed seen in Fig. 10 which displays the fragment excitation energy and neutron multiplicity on the (N_f, Z_f) plane.

A further stringent test of the model is presented in Fig. 11, where the experimental data on the average neutron multiplicity as a function of the fission fragment TKE for $n_{\text{th}} + {}^{235}\text{U}$ [4] are displayed for various mass gates, and compared to the predictions of our model. The description is pretty good, except for those pairs of fragments substantially contributed by the Standard I mode. For the latter, the theoretical neutron multiplicity is too large for the heavy fragment, which is in line with the interpretation of the discrepancies observed above. However, it is to be noted that at the same time the neutron multiplicity of the light partner is underestimated. That is mostly attributed to the impact of the aforementioned bias introduced by the restriction to four dimensions. Within the 5D Brownian shape motion model, Albertsson *et al.* [16] obtained a better description for these fragment pairs. That supports our conjecture that an increase in dimensionality of our model, with the inclusion of independent deforma-

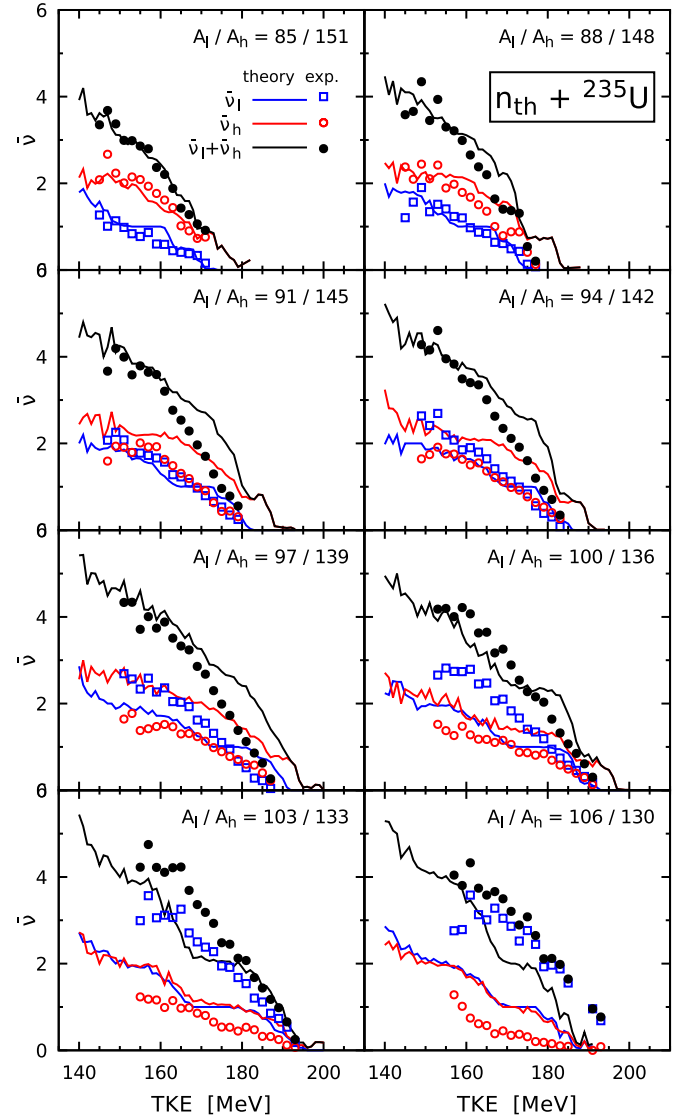


FIG. 11. Average neutron multiplicity as a function of TKE for selected mass pairs, as indicated in the top right corner of each panel. Experimental data of Ref. [4] for the light and heavy fragments separately, and their sum, are compared to the calculation.

tion variables for the light and heavy fragments (a_5 and a_6), will cure most of the deviation of the current theory. This conjecture is supported also by the analysis of the N/Z ratio reported above, where the “6D” model of Ref. [17] based on the same 5D deformation landscape as Ref. [16] achieves a better description than the present 4D model. Nevertheless, we do not exclude that part of the discrepancy observed here may be due to the prescription of excitation energy sharing and charge equilibration at scission. For both aspects we consider for the fragments the macroscopic energy only (i.e., shell effects are omitted). This simplification is planned to be removed in future developments of the model. Furthermore, unlike Ref. [16], we use an approximate formula [7] for the density of states of the deformed fragments, rather than the actual s.p. level densities with the shell effects.

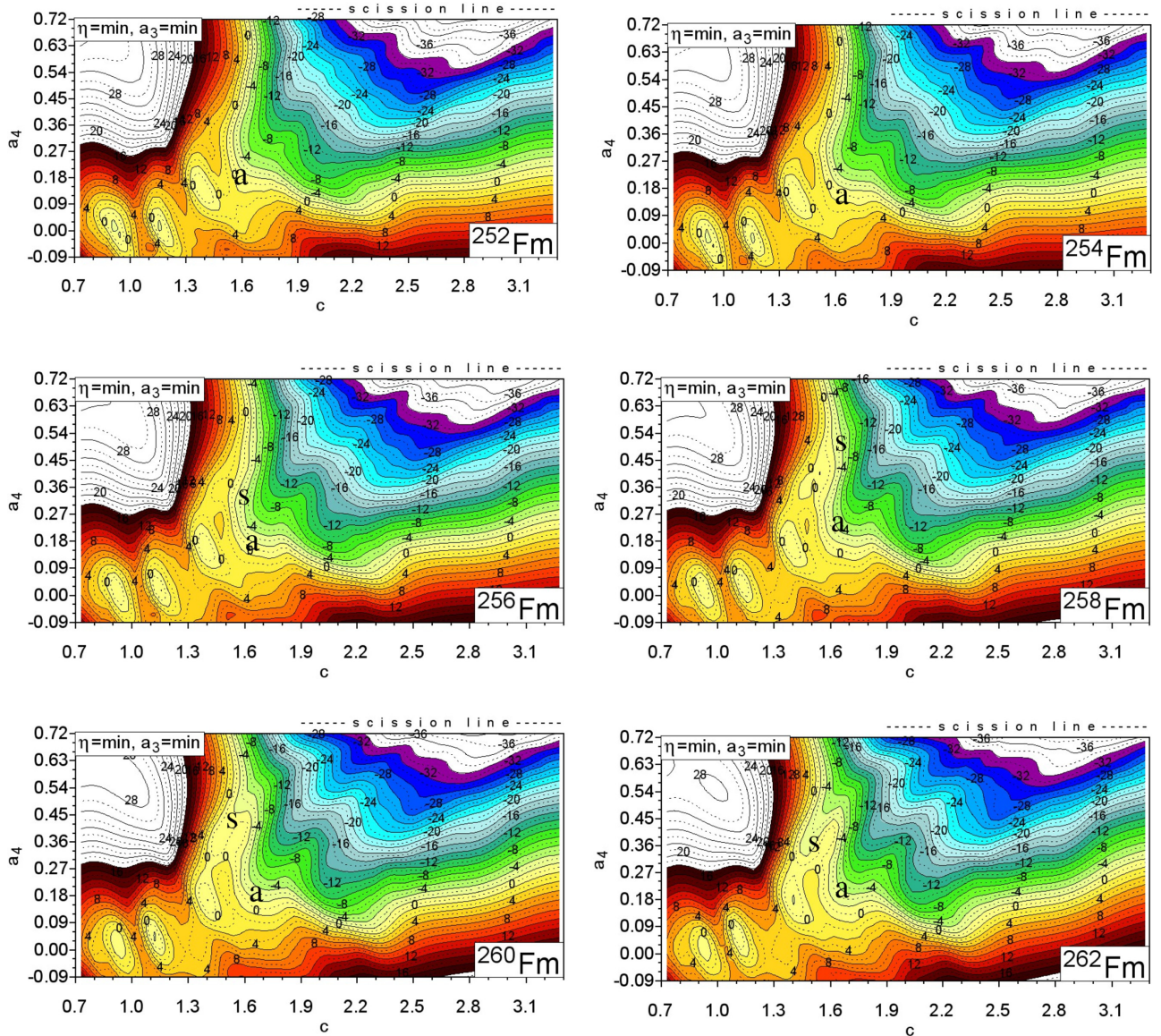


FIG. 12. Potential energy surface of the even-even $^{252-262}\text{Fm}$ isotopes on the (c, a_4) plane. Each point is minimized with respect to the nonaxial (η) and the reflectional (a_3) deformation. The asymmetric **a** and symmetric **s** exit points from the fission barrier are marked.

The present investigation demonstrates that high-fold correlation data, which nowadays are becoming available in experiment, when they are properly propagated in the calculation along the real-time evolution of the fissioning system, are crucial in order to evidence in an unambiguous manner the origin of possible weak points of a model. That is important to guide further development of the theory.

III. APPLICATION TO THE Fm CHAIN

Experiments have well established that the Fm isotopic chain exhibits a very peculiar trend in fragment properties with the size of the fissioning system: the fragment mass distribution changes abruptly from asymmetric for ^{256}Fm to narrow and symmetric in ^{258}Fm [48,49]. At the same time, the TKE has a double-humped shape for the heavier isotope.

This is certainly the best example of bimodal fission. The first theoretical papers providing an explanation for the origin of this observation appeared at the end of the 1980s; they were all based on a static analysis of the PEL (see, e.g., [50]). Thanks to the development of theory and increase in computing resources since then, advanced dynamical calculations are now possible within both the macroscopic-microscopic approach (see Refs. [13,16,51] for 3D, 4D, and 5D models, respectively) and the microscopic self-consistent framework [52]. There is a wide consensus that the sudden transition observed along the isotopic chain of Fm (and of a few more trans-fermium elements) is caused by the proximity of strong shell effects at symmetry in fragments approaching ^{132}Sn with increasing fissioning isotope mass. As obvious from the quoted theoretical papers, a proper description of the mass and TKE yields along the Fm isotopic chain is a good test for any theoretical model.

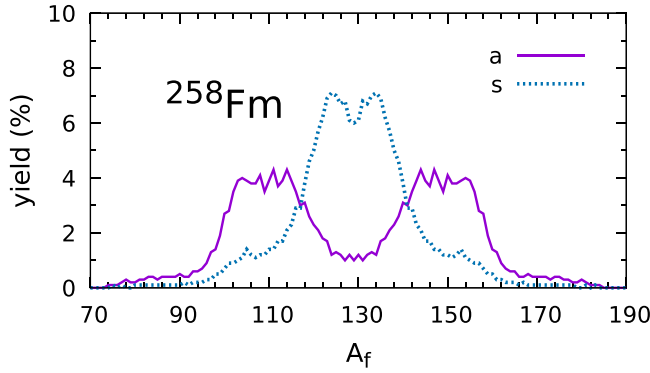


FIG. 13. Fragment mass yield calculated for spontaneous fission of ^{258}Fm corresponding to Langevin trajectories starting from either the asymmetric (**a**) or the compact symmetric (**s**) turning point.

The model described in the present work was used to calculate the fission fragment properties (mass, charge, TKE, postscission neutron multiplicity) along the Fm chain. All parameters were set identical to those employed in the previous section for thermal neutron-induced fission of ^{236}U . The 4D PELs of the even-even $^{252-262}\text{Fm}$ isotopes projected onto the (c, a_4) plane are shown in Fig. 12. Each point of the maps is minimized with respect to the nonaxial (η) and the pearlike (a_3) deformation as for ^{236}U . For the lightest isotopes $^{252,254}\text{Fm}$, the outer saddle point is rather well defined and located at $c \approx 1.5$ and $a_4 \approx 0.18$. Its exit point, denoted **a** in all maps, marks the beginning of a valley which corresponds to asymmetric fission (as seen from the corresponding minimized a_3 ; not shown here). Between ^{256}Fm and ^{258}Fm the pattern in the outer saddle region clearly changes, and still another outer saddle (at $c \approx 1.45$ and $a_4 \approx 0.27$) appears. A new fission valley develops beyond this additional outer barrier in ^{258}Fm . It corresponds to compact symmetric fission configurations and is denoted **s**. The PELs of Fig. 12 suggest that the symmetric valley might attract most of the flux for the heaviest Fm isotopes.

The mass yields calculated for spontaneous fission of ^{258}Fm and corresponding to the starting points **a** and **s** are shown separately in Fig. 13, being respectively asymmetric and symmetric as noted above. The final mass yield is, of course, a weighted sum of these two distributions. The weight suited for **a** and **s** depends on the penetration probability (P_i) of the fission barrier evaluated along the path \mathcal{L}_i , which ends at the i th turning point (**a** and **b**). As deduced from Fig. 12, there are two distinct outer saddle points for the $^{256-660}\text{Fm}$ isotopes, and tentatively also for ^{254}Fm . The heights of the corresponding outer barriers are plotted in Fig. 14. They are almost identical for ^{256}Fm , while in the heavier isotopes, the symmetric barrier is lower than the asymmetric one. This difference in the saddle-point heights indicates that compact symmetric fission should prevail for isotopes heavier than ^{256}Fm . In order to calculate the final mass yield expected for spontaneous fission and compare quantitatively with experiment (wherever available), we proceed as follows.

The final fission fragment yield (Y_{th}) is taken as the weighted sum of the yields Y_a and Y_s obtained using the points

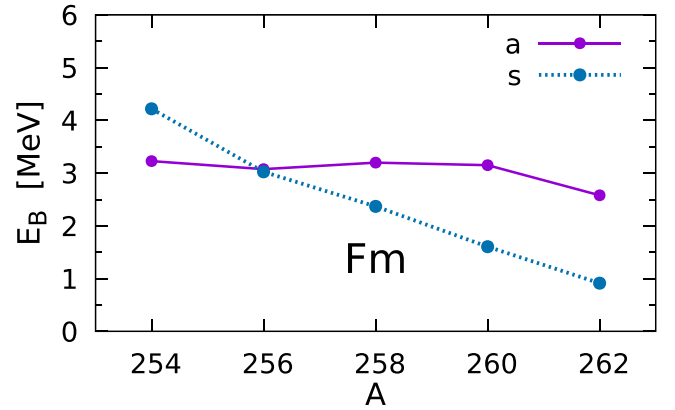


FIG. 14. Second barrier heights along the Fm chain corresponding to the asymmetric **a** and symmetric **s** fission paths as a function of Fm isotope mass.

a and **s** as initial points of the Langevin trajectories:

$$Y_{\text{th}}(A_f) = P_a Y_a(A_f) + P_s Y_s(A_f), \quad (21)$$

where P_a and P_s are the relative probabilities of reaching points **a** and **s** by tunneling of through fission barrier. We follow here the approximation described in Ref. [34] to evaluate P_i .

In the Wentzel-Kramers-Brillouin (WKB) approximation, the barrier penetration probability is given by

$$W_i = \frac{1}{1 + \exp[2S(\mathcal{L}_i)]}, \quad (22)$$

where $S(\mathcal{L}_i)$ is the action integral taken along the \mathcal{L}_i path,

$$S(\mathcal{L}) = \int_{s_l}^{s_r} \sqrt{\frac{2}{\hbar^2} B_{ss}(s) [V(s) - E_0]} ds. \quad (23)$$

Here s_l and s_r are the left and right turning points at the path \mathcal{L} . B_{ss} and $V(s)$ are the collective inertia and potential along the path \mathcal{L} respectively, and E_0 is the ground state energy. The total penetration probability of the barrier is the sum of the probabilities along the asymmetric and symmetric paths. So, the relative populations of the asymmetric and the compact-symmetric valleys are

$$P_a = \frac{W_a}{W_a + W_s} \quad \text{and} \quad P_s = \frac{W_s}{W_a + W_s}. \quad (24)$$

Following the above recipe, the final fission fragment mass yields (thick black line) predicted for spontaneous fission of the even-even $^{246-662}\text{Fm}$ isotopes are shown in Fig. 15. The yield distributions due to path **a** (thin purple line) and to path **s** (dotted blue line) are also displayed for reference. For the lighter $^{254-456}\text{Fm}$ isotopes, the mass yields do not depend on the choice of the starting point, while for the heavier ones they differ significantly. One obtains the asymmetric mass yield (solid line) when starting from the point **a** and the symmetric distributions corresponding to the initial point **s**. The maximum of the asymmetric component in the final distribution is located between $A \approx 146$ and 150 for the heavy fragment depending on fissioning mass, while for the symmetric component, there are two close-lying maxima, with the heaviest

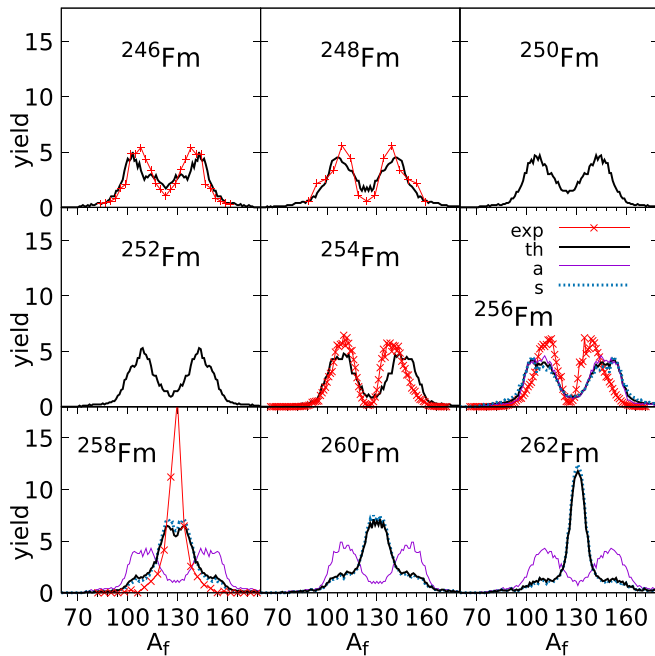


FIG. 15. Fission fragment mass yields along the Fm isotopic chain. The calculation (solid black line) is compared with experimental data for preneutron yields (red +) [53,54] or postneutron yield (red ×) [11,48] depending on availability (the little shift between pre- and postneutron mass distributions is of no importance for the present comparison). The theoretical curves corresponding to the asymmetric (thin purple line) and symmetric (dotted blue line) fission paths are shown separately for reference; see the text.

one is sitting at $A_h = 132$; the light partner is given by the fissioning mass. Comparison between the final calculation and experiment is seen to be pretty good, bearing in mind the simple recipe outlined above. Further improvement requires one to consider the full dynamics of the process starting from, e.g., the second minimum as in Ref. [13] (rather than assuming simple tunneling through each barrier separately). Work in this direction is the scope of future enhancement of the model.

The calculated final fission fragment TKE distribution for spontaneous fission of ^{258}Fm is shown in the top panel of Fig. 16. This weighted TKE yield (thick black full line) can be compared with the experimental data (red histogram) [48]. The TKE yields corresponding to the starting points **a** (thin purple) and **s** (dotted blue) are drawn also. The theoretical result is seen to reproduce very reasonably the measurement. In particular it exhibits the two-humped pattern mentioned in the Introduction. According to the discussion above, for the ^{258}Fm isotope, the contribution from path **s** dominates. In this respect, it is important to note that Fig. 16 suggests that the low-energy component of the TKE distribution originates almost exclusively from path **s** rather than from path **a**. In other words, path **s** has itself a two-humped distribution, i.e., it has contributions from two different modes. This could already been seen in Figs. 13 and 15, where some asymmetric wings appear next to the symmetric peak in the mass distribution of path **s**. The mean TKE as a function of the fission fragment mass is plotted in the bottom part of Fig. 16. It is seen there

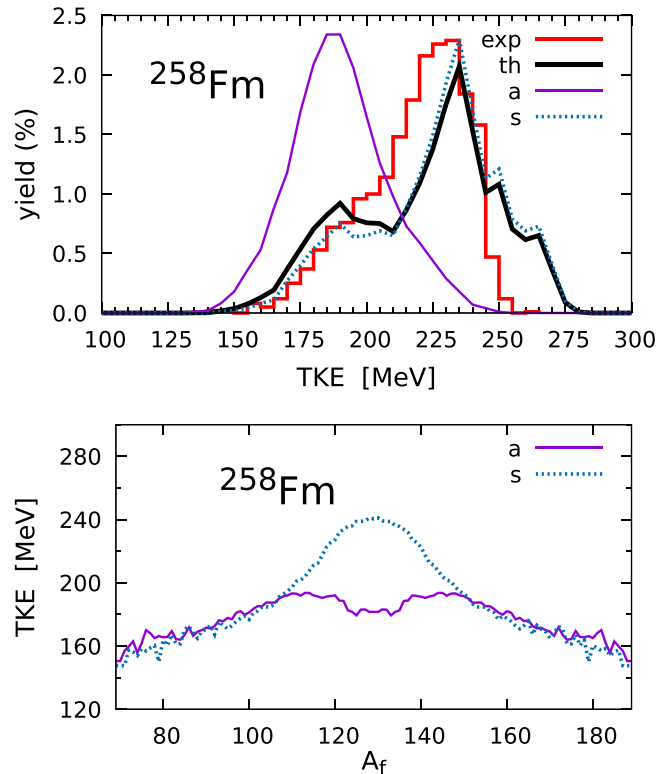


FIG. 16. Top: fission fragment TKE distribution for spontaneous fission of ^{258}Fm . The final calculated distribution is shown with the thick black full line, while the distributions characteristic of paths **a** (thin purple full) and **s** (dotted blue) are displayed for reference. Experimental data (red histogram) are taken from Ref. [48]. Bottom: mean TKE as a function of the fragment mass for paths **a** and **s**.

that for $A_f = 258/2$ the TKE corresponding to the path **s** is about 50% larger than the one related to the path **a**. It shows that in the case **s**, for most symmetric events, one deals with a compact symmetric path. The TKE spectra confirm conclusions drawn from the mass yields comparison: in ^{258}Fm , the compact-symmetric fission predominates.

To get a deeper insight into the above observations and discussion, we consider higher-fold correlations. Figure 17 displays the fragment yield (top) and the elongation of the system just before scission, at the end of the trajectory (bottom) as a function of fragment mass and TKE for spontaneous fission of ^{258}Fm . The upper panel exhibits the dominant symmetric component with $\text{TKE} \approx 234$ MeV (dark blue and red blob) and the small contribution from the asymmetric Standard II mode at $(A_l, A_h) \approx (113, 145)$ and $\text{TKE} \approx 180$ MeV (light blue bands); see also the bottom of Fig. 16. In addition, some slightly less asymmetric component is dragging from the symmetric high-TKE region down to TKEs as low as ≈ 129 MeV. These events correspond to the asymmetric wings of path **s** mentioned above. A further insight can be obtained from the bottom panel of the Fig. 17, which informs us about the elongation close to scission. The dominant symmetric component originating from path **s** is seen to be characterized by the smallest elongation $c \approx 2$ at scission, confirming that it corresponds to a compact symmetric mode. The Standard II

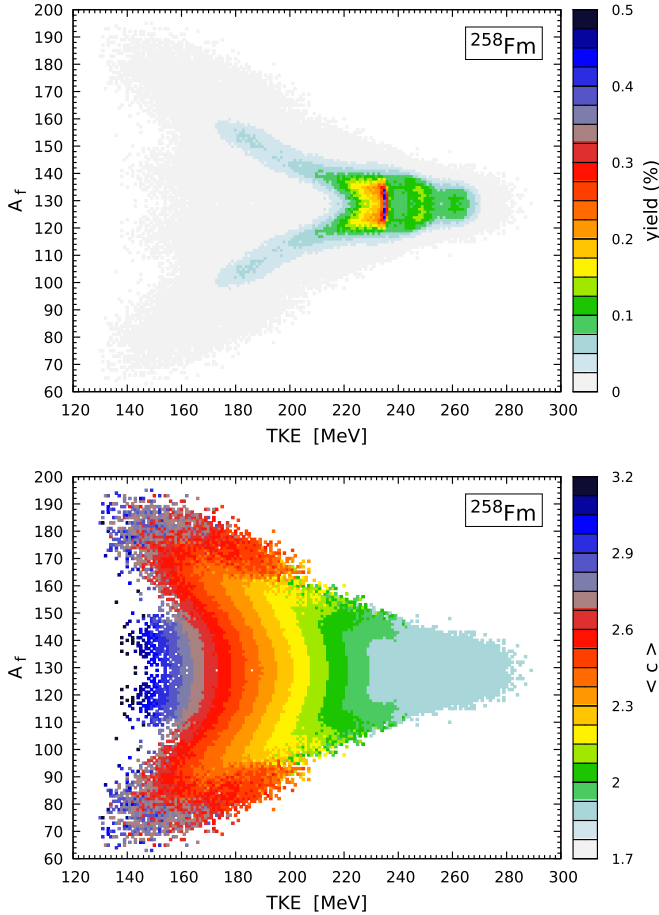


FIG. 17. Fission fragment yields (upper panel) and corresponding average elongation $\langle c \rangle$ close to scission (bottom panel) for spontaneous fission of ^{258}Fm as a function of fragment TKE and mass A_f .

asymmetric mode has a somehow larger mean $c \approx 2.2$ – 2.4 at scission, as expected. But maybe most interesting is that the slightly asymmetric wings dragging from symmetry to very low TKE, which end as distinct blue blobs clearly separated from Standard II, have a mean elongation at scission above $c \approx 2.7$, viz., larger than Standard II. That corroborates that the asymmetric wings from path **s** discussed above do not originate from the Standard II mode due to path **a**, but rather shall be considered as the asymmetric tails of a symmetric elongated mode stemming from path **s**. It is to be noted that these tails dominate the mass distribution of path **s** in ^{256}Fm , while the symmetric compact mode prevails in ^{258}Fm (see purple curves in the corresponding panels of Fig. 15). This can be best understood from a detailed look at Fig. 12, which shows that these two “subpaths” separate at $c \approx 1.7$ and $a_4 \approx 0.54$. The small differences between the PELs of ^{256}Fm and ^{258}Fm drive the system in one or the other subpath (in addition to the influence of the dynamics).

Finally, the predicted postscission neutron multiplicities for spontaneous fission of ^{258}Fm are shown in Fig. 18 as a function of the fragment (N_f , Z_f) isotopic composition. The diagonal purple lines correspond to constant masses. Obvi-

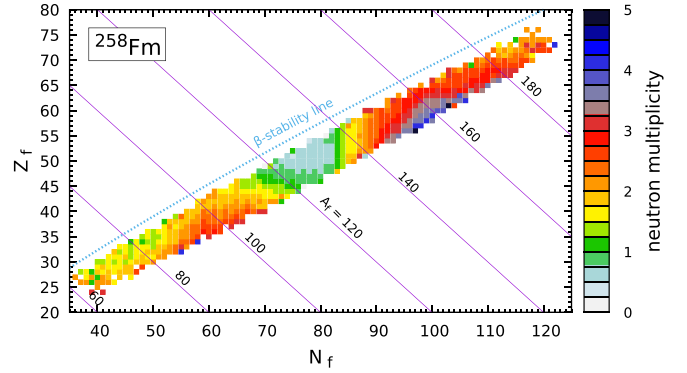


FIG. 18. Postscission neutron multiplicity for spontaneous fission of ^{258}Fm as a function of fragment neutron number N_f and proton number Z_f .

ously, the number of emitted neutrons at a given mass grows with the distance from the β -stability line. For the Standard II mode, the heavy and light fragments emit on the average a comparable number of neutrons, consistent with experimental observation in the region (see, e.g., [55]), although evaporation may be slightly overestimated for the heavy partner (see also Fig. 11). The compact symmetric mode exhibits the lowest postscission multiplicity, only 0.5 neutron on average, in line with the above discussion: the fragments of this mode are close to magic nuclei, poorly excited at scission and which experience very little shape relaxation after scission. The asymmetric wings of the mass distribution of path **s** which we identified above as stemming from an elongated symmetric mode show postscission multiplicity values which are somehow intermediate between those of Standard II and of the compact symmetric mode, while it would be expected that these events exhibit the largest postscission multiplicities. Overall the model thus describes the main trends observed in experiment in the region. The deficiency regarding a more detailed quantitative description is mostly due to the limitation of the theory in terms of full variety of shapes, in particular at scission, of the energy sharing prescription already mentioned above.

IV. CONCLUSIONS

We have proposed the innovative Fourier-over-spheroid (FoS) prescription as a fast and flexible nuclear shape parametrization to model fission by means of four collective coordinates, i.e., elongation, left-right asymmetry, neck size, and nonaxiality. Neglecting nonaxiality from the outer saddle region to scission, we have developed a new 3D Langevin code, based on the FoS, the LSD + Yukawa folded macroscopic-microscopic potential energy landscape, a procedure to account for charge equilibration at scission, and a method to compute the excitation energy available in the primary fragments. Finally, the deexcitation of the latter after scission was computed. Altogether it gives access to a wide palette of observables, treated in a consistent way, which permits one to analyze high-fold correlations. Such information is crucial to evaluate in a unambiguous way the reliability of specific theoretical prescriptions which are often entangled in the intricate fission process.

The model was first tested and tuned to reproduce at best experimental observation from thermal neutron-induced fission of ^{235}U . In a second step, it was applied to fission along the Fm isotopic chain, and seen to explain the famous abrupt transition observed in the fragment properties between ^{256}Fm and ^{258}Fm .

The achievement of the present model is considered to be impressive considering its relative simplicity. Remaining discrepancies are ascribed to limitations mainly in terms of dimensionality of the shape parametrization, restriction to the outer saddle to scission dynamics, charge equilibration and energy sharing recipes at scission, and possibly the neglect of angular momentum. Work to improve the model along these lines is foreseen. Also, the extension of the model to account for multichance fission is underway. This enhancement is very important for calculations of interest in nuclear energy applications. Further calculations for wider mass and excitation energy ranges of the fissioning nucleus, and comparison with experiment wherever available, are in progress in parallel. These are important to constrain more and more the model ingredients, and refine them. Independently of these developments, the model constitutes already a useful tool for various domains where systematic and fast predictions are required. Additionally, the conclusions drawn from its comparison with experiment can be a useful guide for more fundamental theory.

ACKNOWLEDGMENTS

We acknowledge discussions with F. A. Ivanyuk. The authors would like to thank A. Göök and A. Al-Adili for supplying us with some experimental data. This work was supported by the Polish National Science Center (Grant No. 2018/30/Q/ST2/00185) and by the Natural Science Foundation of China (Grants No. 11961131010 and No. 11790325).

APPENDIX: DEFORMATION OF FISSION FRAGMENTS

At the end of each thousand Langevin trajectories, i.e., at scission configuration, one has to determine the deformation parameters of both fission fragments. This procedure has to be repeated several thousand times, so it should be rapid. Knowl-

parent ———
 (c, a_3 , a_4) ———
 (c, a_3 , $a_4=0$) - - - - -
 (c, $a_3=0$, $a_4=0$) ······

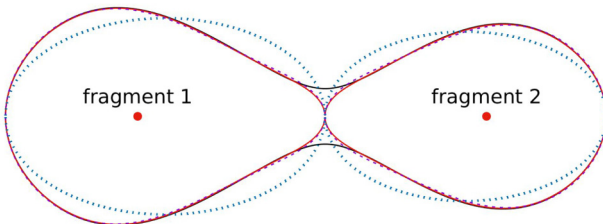


FIG. 19. Shape of the parent nucleus (black line) and the fragments fitted using only the elongation parameter c (dotted line), c and the pearlike deformation a_3 (dashed line), and three deformation parameters c , a_3 , and a_4 (red line).

edge of the fragment deformations is necessary to estimate its deformation energy, which contributes significantly to the fragment excitation energy (13).

Let us assume the fission fragments have the masses A_1 and A_2 , where $A = A_1 + A_2$ is the mass of the parent nucleus described by the profile $\rho^2(z)$, Eq. (1). The following data on the parent nucleus around scission are needed to determine the deformation of the fragments:

$$z_{\min} = -z_0 + z_{\text{sh}}, \quad z_{\text{neck}}, \quad z_{\max} = z_0 + z_{\text{sh}},$$

$$z_{\text{cm}}(1), \quad z_{\text{cm}}(2), \quad \rho^2\left(\frac{z_{\min} + z_{\text{neck}}}{2}\right), \quad \rho^2\left(\frac{z_{\text{neck}} + z_{\max}}{2}\right).$$

The corresponding spherical radii are R_{01} , R_{02} , and R_0 , where $R_{0i} = R_0(A_i/A)^{1/3}$. The fragment elongations are

$$c_1 = \frac{z_{\text{neck}} - z_{\min}}{2R_{01}},$$

$$c_2 = \frac{z_{\max} - z_{\text{neck}}}{2R_{02}}. \quad (\text{A1})$$

One evaluates the reflection asymmetry parameter a_{3i} from the shift of the fragment mass center with respect to its geometrical center:

$$a_{31} = -\frac{2\pi}{3c_1R_{01}} \left[z_{\text{cm}}(1) - \frac{z_{\text{neck}} - z_0 + z_{\text{sh}}}{2} \right],$$

$$a_{32} = -\frac{2\pi}{3c_2R_{02}} \left[z_{\text{cm}}(2) - \frac{z_0 + z_{\text{sh}} - z_{\text{neck}}}{2} \right]. \quad (\text{A2})$$

To determine the a_{4i} deformation of the fragment i one uses the FoS relation:

$$\rho_i^2(0) = \frac{R_{0i}^2}{c_i} f(0) = \frac{R_{0i}^2}{c_i} \left(1 - \frac{4}{3}a_{4i} - \frac{4}{5}a_{6i} - \dots \right), \quad (\text{A3})$$

where

$$\rho_1^2(0) = \rho^2[(z_{\text{neck}} + z_{\max})/2],$$

$$\rho_2^2(0) = \rho^2[(z_{\text{neck}} + z_{\min})/2]. \quad (\text{A4})$$

Assuming that $a_6 = -a_4/10$ (LD energy minimum) one obtains

$$\rho_i^2(0) = \frac{R_{0i}^2}{c_i} \left(1 - \frac{96}{75}a_{4i} \right), \quad (\text{A5})$$

which implies

$$a_{4i} = \frac{75}{94} \left(1 - \frac{c_i}{R_{0i}^2} \rho_i^2(0) \right). \quad (\text{A6})$$

The quality of the shape described above is shown in Fig. 19. It is seen that taking into account the pearlike deformation significantly improves the quality of the fit, while the a_4 deformation has only a tiny effect.

- [1] N. Schunck and D. Regnier, *Prog. Part. Nucl. Phys.* **125**, 103963 (2022).
- [2] H. J. Krappe and K. Pomorski, *Nuclear Fission Theory*, Lecture Notes in Physics Vol. 838 (Springer-Verlag, Berlin, 2012).
- [3] A. N. Andreyev, K. Nishio, and K.-H. Schmidt, *Rep. Prog. Phys.* **81**, 016301 (2018).
- [4] A. Göök, F.-J. Hamsch, S. Oberstedt, and M. Vidali, *Phys. Rev. C* **98**, 044615 (2018).
- [5] A. Al-Adili *et al.*, *Phys. Rev. C* **102**, 064610 (2020).
- [6] M. Caamaño, O. Delaune, F. Farget, X. Derkx, K.-H. Schmidt, L. Audouin, C.-O. Bacri, G. Barreau, J. Benlliure, E. Casarejos, A. Chbihi, B. Fernandez-Dominguez, L. Gaudefroy, C. Golabek, B. Jurado, A. Lemasson, A. Navin, M. Rejmund, T. Roger, A. Shrivastava *et al.*, *Phys. Rev. C* **88**, 024605 (2013).
- [7] D. Ramos, M. Caamaño, F. Farget, C. Rodriguez-Tajes, L. Audouin, J. Benlliure, E. Casarejos, E. Clement, D. Cortina, O. Delaune, X. Derkx, A. Dijon, D. Dore, B. Fernández-Dominguez, G. de France, A. Heinz, B. Jacquot, C. Paradela, M. Rejmund, T. Roger, M.-D. Salsac *et al.*, *Phys. Rev. C* **99**, 024615 (2019).
- [8] J.-F. Martin *et al.*, *Phys. Rev. C* **104**, 044602 (2021).
- [9] Y. Abe, C. Grégoire, and H. Delagrange, *J. Phys. Colloq.* **47**, C4-329 (1986).
- [10] K. Mahata *et al.*, *Phys. Lett. B* **825**, 136859 (2022).
- [11] K.-H. Schmidt, B. Jurado, C. Amouroux, and C. Schmitt, *Nucl. Data Sheets* **131**, 107 (2016).
- [12] Y. Aritomo, S. Chiba, and F. A. Ivanyuk, *Phys. Rev. C* **90**, 054609 (2014).
- [13] M. D. Usang, F. A. Ivanyuk, C. Ishizuka, and S. Chiba, *Sci. Rep.* **9**, 1525 (2019).
- [14] K. Hirose *et al.*, *Phys. Rev. Lett.* **119**, 222501 (2017).
- [15] J. Randrup and P. Möller, *Phys. Rev. C* **88**, 064606 (2013).
- [16] M. Albertsson, B. G. Carlsson, T. Døssing, P. Möller, J. Randrup, and S. Åberg, *Phys. Rev. C* **103**, 014609 (2021).
- [17] P. Möller and T. Ichikawa, *Eur. Phys. J. A* **51**, 173 (2015).
- [18] K. Pomorski, B. Nerlo-Pomorska, J. Bartel, and C. Schmitt, *Acta Phys. B Conf. Suppl.* **8**, 667 (2015).
- [19] C. Schmitt, K. Pomorski, B. Nerlo-Pomorska, and J. Bartel, *Phys. Rev. C* **95**, 034612 (2017).
- [20] K. Pomorski, F. A. Ivanyuk, and B. Nerlo-Pomorska, *Eur. Phys. J. A* **53**, 59 (2017).
- [21] K. Pomorski, A. Dobrowolski, R. Han, B. Nerlo-Pomorska, M. Warda, Z. G. Xiao, Y. J. Chen, L. L. Liu, and J. L. Tian, *Phys. Rev. C* **101**, 064602 (2020).
- [22] K. Pomorski, J. M. Blanco, P. V. Kostyukov, A. Dobrowolski, B. Nerlo-Pomorska, M. Warda, Z. G. Xiao, Y. J. Chen, L. L. Liu, J. L. Tian, X. Y. Diao, and Q. H. Wu, *Chin. Phys. C* **45**, 054109 (2021).
- [23] L. L. Liu, Y. J. Chen, X. Z. Wu, Z. X. Li, Z. G. Ge, and K. Pomorski, *Phys. Rev. C* **103**, 044601 (2021).
- [24] P. V. Kostyukov, A. Dobrowolski, B. Nerlo-Pomorska, M. Warda, Z. G. Xiao, Y. J. Chen, L. L. Liu, J. L. Tian, and K. Pomorski, *Chin. Phys. C* **45**, 124108 (2021).
- [25] K. Pomorski, B. Nerlo-Pomorska, and J. Bartel, *Phys. Scr.* **92**, 064006 (2017).
- [26] K. Pomorski and B. Nerlo-Pomorska, *Acta Phys. Pol. B Suppl.* **16**, 4-A21 (2023).
- [27] S. G. Nilsson, C. F. Tsang, A. Sobiczewski, Z. Szymański, S. Wycech, C. Gustafson, I.-L. Lamm, P. Möller, and B. Nilsson, *Nucl. Phys. A* **131**, 1 (1969).
- [28] K. Pomorski and J. Dudek, *Phys. Rev. C* **67**, 044316 (2003).
- [29] A. Dobrowolski, K. Pomorski, and J. Bartel, *Comput. Phys. Commun.* **199**, 118 (2016).
- [30] V. M. Strutinsky, *Nucl. Phys. A* **95**, 420 (1967); **122**, 1 (1968).
- [31] J. Bardeen, L. N. Cooper, and J. R. Schrieffer, *Phys. Rev.* **108**, 1175 (1957).
- [32] A. Gózdź and K. Pomorski, *Nucl. Phys. A* **451**, 1 (1986).
- [33] S. Piłat, K. Pomorski, and A. Staszczak, *Z. Phys. A* **332**, 259 (1989).
- [34] K. Pomorski, A. Dobrowolski, B. Nerlo-Pomorska, M. Warda, J. Bartel, Z. G. Xiao, Y. J. Chen, L. L. Liu, J. L. Tian, and X. Y. Diao, *Eurphys. J. A* **58**, 77 (2022).
- [35] B. Nerlo-Pomorska, K. Pomorski, J. Bartel, and K. Dietrich, *Phys. Rev. C* **66**, 051302 (2002).
- [36] J. Bartel, B. Nerlo-Pomorska, K. Pomorski, and A. Dobrowolski, *Comput. Phys. Commun.* **241**, 139 (2019).
- [37] P. P. Dyachenko, B. D. Kuzminov, and M. Z. Tarasko, *Sov. J. Nucl. Phys.* **8**, 165 (1969).
- [38] M. Verriere, N. Schunck, and D. Regnier, *Phys. Rev. C* **103**, 054602 (2021).
- [39] JENDLLibrary, <http://www.ndc.jaea.go.jp/index.html>.
- [40] M. Caamaño *et al.*, *J. Phys. G Nucl. Part. Phys.* **38**, 035101 (2011), and references therein.
- [41] D. Ramos *et al.*, *Phys. Rev. C* **107**, L021601 (2023).
- [42] F. G. Kondev, M. Wang, W. J. Huang, S. Naimi, and G. Audi, *Chin. Phys. C* **45**, 030001 (2021).
- [43] H. Delagrange *et al.*, *Z. Phys. A* **323**, 437 (1986).
- [44] I. Dostrovsky, Z. Fraenkel, and G. Friedlander, *Phys. Rev.* **116**, 683 (1959).
- [45] S. Oberstedt *et al.*, *Nucl. Data Sheets* **119**, 225 (2014).
- [46] C. Schmitt and P. Moller, *Phys. Lett. B* **812**, 136017 (2021).
- [47] C. Böckstiegel *et al.*, *Nucl. Phys. A* **802**, 12 (2008).
- [48] E. K. Hulet *et al.*, *Phys. Rev. Lett.* **56**, 313 (1986).
- [49] E. K. Hulet *et al.*, *Phys. Rev. C* **40**, 770 (1989).
- [50] S. Ówiok, P. Rozmej, A. Sobiczewski, and Z. Patyk, *Nucl. Phys. A* **491**, 281 (1989).
- [51] Y. Miyamoto, Y. Aritomo, S. Tanaka, K. Hirose, and K. Nishio, *Phys. Rev. C* **99**, 051601(R) (2019).
- [52] D. Regnier, N. Dubray, and N. Schunck, *Phys. Rev. C* **99**, 024611 (2019).
- [53] C. Romano, Y. Danon, R. Block, J. Thompson, E. Blain, and E. Bond, *Phys. Rev. C* **81**, 014607 (2010).
- [54] D. C. Hoffman, J. B. Wilhelmy, J. Weber, W. R. Daniels, E. K. Hulet, R. W. Loughheed, J. H. Landrum, J. F. Wild, and R. J. Dupzyk, *Phys. Rev. C* **21**, 972 (1980).
- [55] J. Gindler, *Phys. Rev. C* **19**, 1806 (1979).